Decoupling the Dynamics of Zinc Hydroxide Sulfate Precipitation/Dissolution in Aqueous Zn–MnO 2 Batteries by Operando Optical Microscopy: A Missing Piece of the Mechanistic Puzzle

Louis Godeffroy, Ivette Aguilar, Jérôme Médard, Dominique Larcher, Jean-marie Tarascon, Frédéric Kanoufi

Decoupling the dynamics of zinc hydroxide sulfate precipitation/dissolution in aqueous Zn-MnO_2 batteries by *operando* optical microscopy: A missing piece of the mechanistic puzzle

*Louis Godeffroy,[1,‡] Ivette Aguilar,[2,4,‡] Jérôme Médard,[1] Dominique Larcher,[3,4] Jean-Marie Tarascon,[2,4] and Frédéric Kanoufi[1]**

Louis Godeffroy, Jérôme Médard, Frédéric Kanoufi
Université Paris Cité, ITODYS, CNRS, F-75013 Paris, France.
E-mail: **frederic.kanoufi@u-paris.fr**

Ivette Aguilar, Jean-Marie Tarascon
Collège de France, Chaire de Chimie du Solide et de l'Energie (CSE), 75005 Paris, France.

Dominique Larcher
Université de Picardie Jules Verne, Laboratoire de Réactivité et Chimie des Solides (LRCS), 80000 Amiens, France.

Ivette Aguilar, Dominique Larcher, Jean-Marie Tarascon
Réseau sur le Stockage Electrochimique de l'Energie (RS2E), 80000 Amiens, France.

Keywords: aqueous batteries, zinc ion batteries, Zn-MnO_2 batteries, optical microscopy, electrodeposition

Abstract. Energy storage provides flexibility to an energy system and is therefore key for the incorporation of renewable energy sources such as wind and solar into the grid. Aqueous Zn-MnO_2 batteries are promising candidates for grid-scale applications due their high theoretical capacity (616 mAh g^{-1}) and the abundance of their components in the Earth's crust. However, they suffer from low cyclability, which is probably linked to the dramatic pH variations induced by the electrochemical conversion of MnO_2. These pH variations are known to trigger the precipitation/dissolution of zinc hydroxide sulfate ($Zn_4(OH)_6SO_4.xH_2O$, ZHS), which might have an influence on the conversion of MnO_2. Herein, optical reflectometry is used to image and quantitively monitor the MnO_2 electrode's charge and discharge *in situ* and under operation. It emphasizes how solid-phase ZHS rules the dynamics of both charge and discharge, providing a comprehensive picture of the mechanism at play in aqueous Zn-MnO_2 batteries. If the precipitation of ZHS might impede the MnO_2 electrode's discharge, it is a crucial pH buffer delaying the occurrence of the competing oxidation of water on charge.

1. Introduction

Designing safe and sustainable batteries is paramount for the transition from fossil to renewable energy sources. For instance, by storing excess solar energy during daytime and restoring it during nighttime, it could be used much more efficiently.[1,2] However, the most widespread batteries, namely Li-ion batteries (LIBs), are not quite suitable for grid-scale applications due to their high cost and the scarcity of their components.[1] In this respect, aqueous Zn-MnO_2 batteries provide an interesting alternative to LIBs as Zn and Mn are more abundant in the Earth's crust than Li and Co for example. Moreover, these batteries work in aqueous electrolytes, making them safer than most LIBs which work in flammable organic electrolytes.[3–9]

However, aqueous Zn-MnO_2 batteries have a poor cyclability, which is difficult to optimize as the charge storage mechanism of this system is still not fully understood.[3–9] A typical galvanostatic charge-discharge cycle of an aqueous Zn-MnO_2 battery is presented in **Figure 1**a. As in most previous works, two plateaus are observed during charge and discharge. These plateaus were often attributed to Zn^{2+} insertion/extraction into/out of MnO_2,[10–20] H^+ insertion/extraction,[21–24] but they could also reveal MnO_2 electrodissolution/electrodeposition,[25–33] or combinations of the latter phenomena.[27,34–40]

From the point of view of the electrode material, most studies discuss complex composites of carbon and chemically synthesized MnO_2 particles of a specific phase (e.g., α-MnO_2, β-MnO_2, λ-MnO_2…). However, if we admit that the electrodeposition/electrodissolution of MnO_2 is the main pathway for charge storage, the phase control offered by chemical synthesis will be quickly lost. It thus seems relevant to propose, as in some recent examples,[24,29,30,38] another approach focusing on the control and understanding of the electrodeposition of MnO_2.

From the analytical point of view, most structural and mechanistic conclusions concerning the electrochemical conversion of MnO_2 were drawn from results obtained by a single analytical technique, which might not be suitable to grasp the mechanism in all its complexity. X-ray diffraction (XRD), for example, only allows to probe well-organized compounds. Therefore, it is practically blind to electrodeposited MnO_2, which exhibits only short-range order,[41,42] as well as to potential amorphous precipitates. This is problematic as zinc hydroxides such as $Zn_4(OH)_6SO_4.xH_2O$ (ZHS), which are expected to precipitate upon MnO_2 electrodissolution (see **Equation 1 and 2**) or H^+ insertion,[21–25,31,32,43] might not always appear in a crystalline

form, thus hindering a comprehensive mechanistic analysis. Moreover, the temporal resolution of laboratory XRD (or spectroscopic techniques) might not be high enough to probe the competing dynamics of MnO_2 electrodissolution and ZHS precipitation.

$$MnO_{2(s)} + 2H_2O + 2e^- \rightarrow Mn^{2+}_{(aq)} + 4HO^-_{(aq)} \quad (1)$$

$$4Zn^{2+}_{(aq)} + 6OH^-_{(aq)} + SO^{2-}_{4(aq)} + xH_2O \rightarrow Zn_4(OH)_6SO_4.xH_2O_{(s)} \quad (2)$$

Although not deeply inspected in the literature to the best of our knowledge, the role of ZHS is likely equally crucial during charge. The electrolyte acidification accompanying MnO_2 electrodeposition should yield ZHS dissolution. This step may then play an important role in the local buffering of the pH close to the electrode. The control of the electrolyte pH is also important during charge as recently highlighted through Pourbaix diagram analyses.[24,44] A pH buffering may favor MnO_2 electrodeposition over the competing oxidation of water.

Optical microscopy has emerged in the last decade as a promising tool to image and also quantify, and thus mechanistically unravel *in situ*/*operando* electrochemical processes related to energy storage.[45–47] In Zn-ion batteries, it was mostly devoted to the imaging of the Zn anode, enabling the localization of the nucleation sites of Zn dendrites with nanometer precision.[48] Regarding cathode materials, mostly Co-oxides were investigated by different optical microscopies.[49–52] They could evidence Li^+ insertion/extraction during individual nanoparticle cycling,[49,50] map the Li^+ front lines within a microparticle,[52] or probe the volumetric expansion/shrinking of a microparticle associated to its charging/discharging.[51]

In this study, optical reflectometry is used to monitor *operando* the preparation of the MnO_2 electrode in an aqueous Zn-MnO_2 battery environment and its further operation in subsequent charge-discharge cycles. Various *ex situ* structural and chemical analyses (ellipsometry, inductively coupled plasma-mass spectrometry (ICP-MS), X-ray diffraction (XRD), X-ray photoelectron spectroscopy (XPS), and Fourier transform-infrared reflection-absorption spectroscopy (FT-IRRAS)) of the electrode are also proposed to identify the materials formed during charge and discharge. Complemented by such *ex situ* analyses, it is shown herein how optical reflectometry enables an *in situ* quantitative evaluation of the dynamics of MnO_2 and ZHS deposition/dissolution associated to the electrochemical conversion of MnO_2. Once made quantitative, optical reflectometry is also employed as an imaging technique to resolve

local electrochemical currents associated to MnO_2 electrodeposition around a ZHS microparticle, thus allowing to decipher the role of ZHS on charge.

2. Results and discussion

2.1. Operating principle

This study consists, as depicted in Figure 1b and c, in optically imaging the positive current collector (here a reflective Au surface) during the initial electrodeposition of MnO_2 from Mn^{2+} in the electrolyte, and subsequent charge-discharge cycles. Cycling is achieved either by cyclic voltammetry (CV) or in galvanostatic mode, in electrolytes of compositions comparable to those used in the literature, except that the concentration of Mn^{2+} ions is 100 times lower (2 mM $MnSO_4$ instead of 0.2 M) in order to limit the growth rate and thickness of the MnO_2 film.

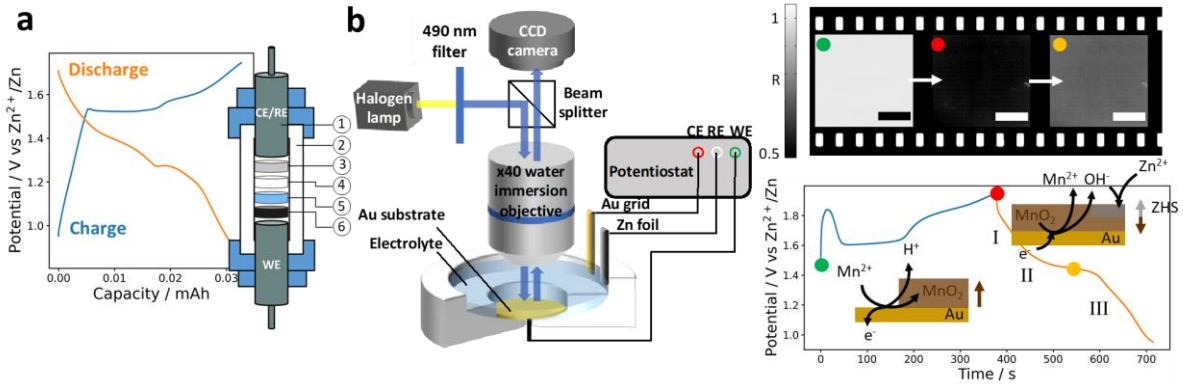

Figure 1. a) Galvanostatic charge-discharge cycle (7th cycle) obtained in a two-electrode ½'' Swagelok cell (scheme on the right: 1 stainless steel plunger, 2 cell body, 3 anode: Zn disk, 4 glass fiber separator, 5 electrolyte: 0.2 M $MnSO_4$ + 2 M $ZnSO_4$, 6 cathode mixture: 6 mg of carbon powder; current: 30 µA, i.e. a C-rate of 1C). b) Scheme of the *operando* optical reflectometry setup used to probe MnO_2 conversion on a Au current collector during CV or galvanostatic charge-discharge. Reflectivity images (enlarged in **Figure SI1-1**) taken at different stages of a galvanostatic charge-discharge cycle (3rd cycle, current: 2 µA (9C), electrolyte: ZHS-saturated 2 mM $MnSO_4$ + 2 M $ZnSO_4$, scale bars: 20 µm), and schematic illustration of the material deposition mechanism optically probed during the experiment.

A typical galvanostatic charge-discharge cycle performed under optical monitoring in a 2 mM $MnSO_4$-containing electrolyte is presented in Figure 1b. It shows a behavior similar to that observed at a higher Mn^{2+} concentration in a Swagelok cell (Figure 1a). The two characteristic plateaus with bump are detected, although at slightly different potentials in agreement with the increase of oxidation potential with decreased Mn^{2+} content and higher cycling rate.[21,30] Optical images of the electrode surface are acquired continuously (at 0.5

frame per second) during the experiment. They are mathematically converted into reflectivity, R, images, as explained in the "Material and experimental methods" section and SI, section 2, which represent the relative variation of optical contrast of the imaged surface. Typical reflectivity images, taken at different states of (dis)charge, are given in Figure 1b (enlarged versions in Figure SI1-1). The optical monitoring then provides a dynamic measurement of the local reflectivity, R, of the electrode surface during charge and discharge.

During charge, the electrode darkens as a MnO_2 film grows on top of it, making it less reflective (the reflectivity, R, decreases) than the original Au surface. During discharge, the electrode brightens again (R increases), already suggesting MnO_2 electrodissolution rather than other types of conversion. By monitoring the darkening/brightening (the reflectivity, R) of the electrode surface, one can then track the accumulation/removal of material onto/from it. First, a qualitative analysis of the optical images is proposed during CV experiments.

2.2. Cyclic voltammetry – qualitative analysis

For the qualitative analysis, two different electrolytes are compared: the usual electrolyte for galvanostatic cycling in a Swagelok cell (diluted in Mn^{2+} to limit the thickness of the MnO_2 film, see above) i.e., 2 mM $MnSO_4$ + 2 M $ZnSO_4$ (pH ≈ 3.8), and ZHS-saturated 2 mM $MnSO_4$ + 2 M $ZnSO_4$ (pH ≈ 5.2, $[Zn^{2+}]$ = 2.14 M (ICP-MS)). The latter should be more representative of the solution composition reached in a Swagelok cell. Indeed, since the electrolyte volume contained in a Swagelok cell is much smaller than in the *operando* optical reflectometry cell (300 µL vs 10 mL), a more rapid pH increase is expected upon MnO_2 electrodissolution in a Swagelok cell.

Although the electrochemical behavior of cells is often discussed in light of repetitive (stable) charge-discharge cycles, apprehending the initial electrodeposition of MnO_2 onto the current collector is fundamental in aqueous Zn-MnO_2 batteries. Indeed, even if the battery initially contains MnO_2 particles in the cathode mixture and is started on discharge, several groups have shown that the presence of Mn^{2+} ions in the electrolyte is mandatory to achieve better cyclability. This is because a constant amount of Mn^{2+} benefits MnO_2 electrodeposition during subsequent charges.[21,24] For this reason, we propose to observe the system's behavior during the first cycle, starting on charge from a bare electrode. The first cycle of representative CVs obtained in both electrolytes are given in **Figure 2**a and d. Subsequent cycles have also been recorded (**Figure SI3**). They show identical to very similar behaviors.

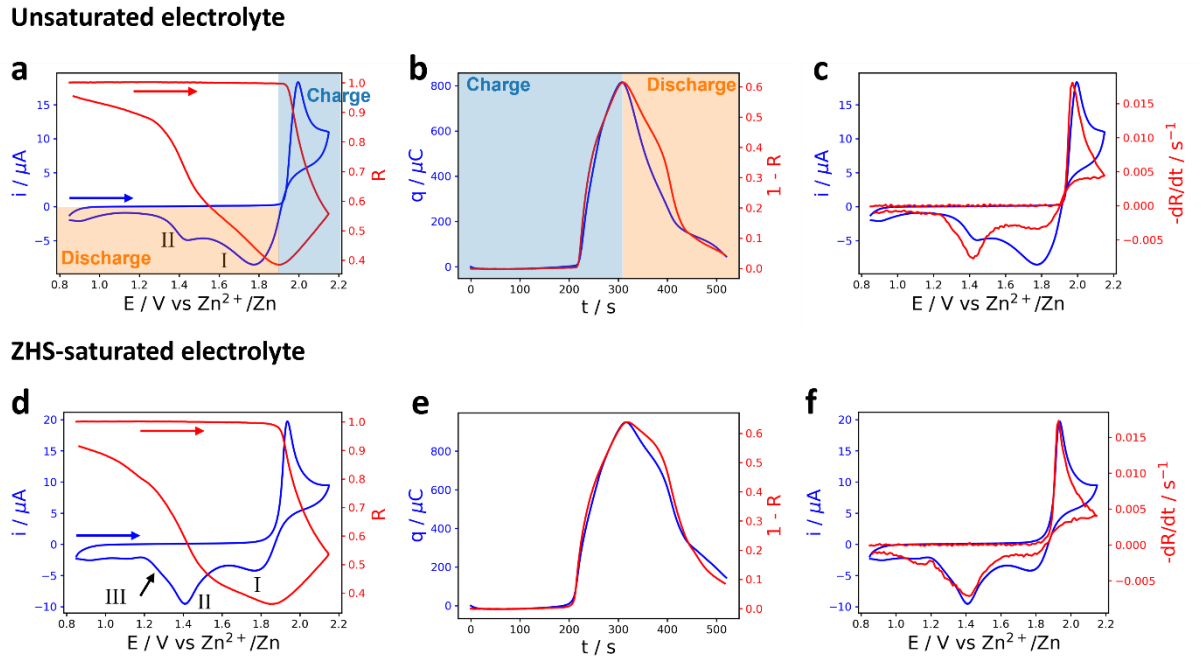

Figure 2. Electrochemical CV (blue line) and corresponding reflectivity, R, variation (red line) of a Au substrate (average value over ≈ 1000 μm^2) obtained in a) unsaturated and d) ZHS-saturated 2 mM $MnSO_4$ + 2 M $ZnSO_4$ (scan rate: 5 mV s^{-1}). b) and e) Unfolded and integrated representation of the CVs showing the charge (light blue area) then discharge (orange area) processes with corresponding electrochemical charge (q, integrated from the electrochemical current, blue line) and transmittivity (1-R, red line) variations with time. c) and f) Electrochemical CVs (blue line) and corresponding optical CVs (red line).

Optical images of the Au current collector are recorded simultaneously and converted into reflectivity images. A typical movie of the current collector reflectivity recorded during the CV performed in the ZHS-saturated electrolyte is provided as **Supplementary Video 1**. The changes in reflectivity, R, during the charge and discharge processes can be rationalized as changes in material deposition onto the reflective Au electrode based on Fresnel's treatment of optical reflections at multiple interfaces: a decrease/increase of the reflectivity relates to a relative accumulation/removal of material (of lower permittivity than Au) onto/from the electrode surface. In order to monitor the cycling of MnO_2 electrodes, a first model considering the growth of a single-component layer (of MnO_2) onto a Au substrate is used (see SI, section 2). In the limit of the deposition of thin MnO_2 layers (up to ca. 20 nm, **Figure SI2**a), provided by charging from an electrolyte containing only 2 mM $MnSO_4$, the reflectivity of the Au substrate should vary linearly with the thickness of the MnO_2 layer, δ_{MnO2}, as:[47,53,54]

$$1 - R = \delta_{MnO_2} n_{sol} \frac{8\pi}{\lambda} Im\left(\frac{n_{MnO_2}^2 - n_{Au}^2}{n_{sol}^2 - n_{Au}^2}\right) \quad (3)$$

where n_{sol}, n_{MnO2} and n_{Au} represent the complex refractive indices of the electrolytic solution, the MnO_2 layer and the Au surface (given in the caption of Figure SI2), Im the imaginary part of the corresponding fraction, and λ the wavelength of the incident light, respectively. The reflectivity variations for thicker MnO_2 deposits can also be evaluated (see SI, section 2). Worth mention, that coatings composed of multiple components (e.g., MnO_2 and ZHS) can also be modelled as will be discussed below.

The reflectivity images are generally homogeneous, as shown in Figure 1b (enlarged versions in Figure SI1-1). This suggests a homogeneous transformation of the Au surface, at least within the 0.5 µm optical lateral resolution evaluated experimentally (**Figure SI1-2**). It means that within this 0.5 µm resolution, MnO_2 is not growing in a dendritic fashion. Hence, average values of R (over ≈ 1000 μm^2) are considered first. The evolution of the average value of R during the CVs in both electrolytes are also presented in Figure 2a and d.

Noteworthy, in CV experiments, charge and discharge are performed at variable potential and current. As illustrated by the blue-colored region in Figure 2a, the charge step lasts as long as the current is positive i.e., during the whole forward scan and the first part of the backward scan. The discharge step (orange region in Figure 2a) starts during the backward scan when the current becomes negative. For clarity, the CVs are also presented in Figure 2b and e in their unfolded and integrated form (charge vs time), showing more distinctly the charge and discharge steps.

During the first forward (oxidation) scan, the reflectivity of the Au substrate, R, decreases concomitantly to the appearance of an oxidation peak in the CVs. This confirms that the oxidation of Mn^{2+} ions from the electrolyte results in the deposition of a Mn-oxide onto the Au electrode. This Mn-oxide is identified as being MnO_2 from the > 95% faradaic efficiency of the process (determined by ICP-MS, **Table SI4-1**). According to **Equation 3**, 1-R scales as the amount of deposited material, and therefore as the amount of charge, q, injected during the electrodeposition/electrodissolution (see SI, section 2). The electrochemical charge, q, exchanged during the CV is then compared to 1-R in Figure 2b and e and both quantities match perfectly during the whole charge (up to ≈ 300 s).

During discharge, along the reverse scan, two reduction peaks are observed in the unsaturated electrolyte (Figure 2a), respectively at 1.8 (I) and 1.4 V (II). In the ZHS-saturated electrolyte (Figure 2d), peak I decreases in intensity (and amount of charge) for the benefit of peak II. In addition, a shoulder (III) appears at 1.3 V. These three features are consistent with the ones observed during galvanostatic discharge in the same conditions (Figure 1b). After a short discharge plateau at ca. 1.7-1.8 V (peak I), a larger discharge plateau is detected at ca. 1.4 V (peak II), followed by a last sloping discharge plateau at 1.3 V matching with shoulder III. According to the literature, peak I should correspond to the reduction of MnO_2 in an acidic environment,[27,29,55–57] which is usually not encountered in a Swagelok cell due to its small volume, and whose contribution can be strongly attenuated by saturating the electrolyte with ZHS (see above).

The reflectivity changes during the backward scan, better visualized in the unfolded charge-time representation of the CVs (Figure 2b and e), do not match the evolutions of q anymore, except at the very end (t > 400 s) in the unsaturated electrolyte. This means that the discharge dynamics (electron injection) does not track the dynamics of MnO_2 dissolution. The better match in the unsaturated electrolyte at the end of the discharge means that overall, the discharge is consistent with the dissolution of MnO_2 into soluble Mn^{2+}. The reflectivity also almost returns to 1 and the charge to 0, indicating that nearly all the MnO_2 deposited during the forward (oxidation) scan is dissolved during the reverse (reduction) scan, which is further confirmed by *ex situ* ellipsometry (**Figure SI5**a).

The differences in the charge and reflectivity dynamics are also visible in differentiated variables such as the electrochemical current and equivalently for the optical signal, -dR/dt, hereafter denoted as optical current. If the reductive electrochemical current expresses the rate of charge injection (e.g., via Equation 1) for the reduction of MnO_2, the optical current expresses the apparent rate of material deposition (-dR/dt > 0) or dissolution (-dR/dt < 0) on the electrode. For the unsaturated electrolyte, the electrochemical and optical currents are compared in Figure 2c. When the oxidation peak currents of both CVs are matched, significant differences during discharge are revealed. During the first reduction peak at 1.8 V (peak I), the optically inferred apparent dissolution rate is smaller than suggested by the electrochemical current, and vice versa during the second reduction peak at 1.4 V (peak II).

These discharge/dissolution rate mismatches are also detected when several CV cycles are performed (Figure SI3a).

The small dissolution rate compared to the charge transfer rate measured during peak I suggests an overall electrodissolution of MnO_2, but with low faradaic efficiency. It can have different explanations pointing the intervention of concurrent paths, either an electron transfer path, a chemical material deposition path, or a combination of both. The competing electron transfer path could, for example, be the reduction of MnO_2 into MnOOH. Owing to the ≈ 8% decrease in refractive index when going from MnO_2 to MnOOH,[58] the full conversion of MnO_2 into MnOOH would yield a reflectivity variation of ≈ 0.1. If this conversion could explain the reflectivity variations measured during peak I, it cannot explain the reflectivity variations measured during the entire discharge, and more so as MnOOH is expected to disproportionate into soluble Mn^{2+} and MnO_2 in the investigated pH range.[24,44] Moreover, the reductive intercalation of Zn^{2+} ions would also yield some apparent material accumulation on the electrode, but this process should be self-limited to the Au-MnO_2 interface since $ZnMn_2O_4$ is not electroactive.[59] It is more likely that a chemically formed material kinetically precipitates on the electrode (at the MnO_2-electrolyte interface) during peak I. This hypothesis is supported by experiments where the potentiostat is stopped at 1.7 V in the backward scan (shortly after peak I) while images of the surface are still continuously acquired. As soon as the potentiostat is stopped, the optical current becomes positive (and stays positive for > 100 s), meaning that material continuously accumulates on the substrate at open circuit although no charge is injected anymore (**Figure SI6**). As the overall process occurring during peak I is an apparent dissolution, the contribution of the competing reactions is lower than (almost compensates) the overall dissolution of MnO_2. It is however difficult at this stage to evaluate the contribution of each process: (1) the electrodissolution into Mn^{2+}, (2) the reduction into MnOOH or intercalation, and (3) the chemical precipitation of another material.

In the ZHS-saturated electrolyte, the same mismatch between the electrochemical and optical CVs is observed in the region of peak I at 1.8 V (Figure 2f), and the same competing paths could be invoked. However, in the ZHS-saturated electrolyte, the release of HO^- ions during MnO_2 electrodissolution should allow for a supersaturation of ZHS near the electrode surface and thus favor its precipitation. The precipitation of ZHS is widely acknowledged in this kind of systems,[21–23,25,31,43] but its presence on the electrode surface has only been revealed at the

latest stages of the discharge process and particularly during the second discharge plateau. The qualitative analysis above suggests it also occurs at the beginning of the discharge (peak I). To confirm this suggestion, we propose, based on complementary chemical and structural analyses, a more quantitative analysis of the reflectivity results in the following sections.

2.3. Cyclic voltammetry – quantitative analysis in the ZHS-saturated electrolyte

2.3.1. Analysis of the charge

The CV and reflectivity data from Figure 2d-f is now interpreted in terms of electrochemical charge and deposited/dissolved mass, providing information similar to that obtained by an optical Surface Plasmon Resonance (SPR) sensorgram[60] or by an Electrochemical Quartz Crystal Microbalance (EQCM). In the field of EQCM, a common analysis consists in plotting the mass change (calculated from the quartz crystal's frequency change) against the electrochemical charge.[23,31] By virtue of Faraday's law, the slope of this plot is proportional to the molar mass of the electrodeposited/electrodissolved compound, thus enabling its identification. Similarly to the frequency change of an EQCM, the reflectivity change of the Au substrate can also be converted into a mass change. First, the experimental reflectivity change is expected to follow Equation 3 for a single-component film, meaning that at a constant wavelength the complex refractive indices on the right-hand side of Equation 3 are constant. Then, 1-R is expected to vary linearly with the MnO_2 film thickness. The experimental reflectivity is then converted into an apparent MnO_2 thickness, δ_{app}, using a calibration factor, C_f, determined by *ex situ* ellipsometry at the end of the charge, from:

$$1 - R = \delta_{MnO_2} n_{sol} \frac{8\pi}{\lambda} \mathrm{Im}\left(\frac{n_{MnO_2}^2 - n_{Au}^2}{n_{sol}^2 - n_{Au}^2}\right) = C_f \delta_{app} \quad (4)$$

Then, the optically inferred thickness, δ_{app}, is converted into an apparent mass, m_{app}, by multiplying it by ρ_{app}, the apparent density of the MnO_2 film, and S, the geometric surface area of the Au electrode in contact with the solution (S = 0.16 cm^2 for the experiment shown in Figure 2d-f):

$$m_{app} = \delta_{app} \rho_{app} S. \quad (5)$$

The optically inferred mass of equivalent MnO_2 deposit, m_{app}, is then compared to the electrochemical charge, q, integrated from the CV, separated into charge and discharge as

presented in **Figure 3**. During charge (Figure 3a), the deposited mass linearly increases with the amount of injected charge, in line with the faradaic nature of the electrodeposition. Together with the overall faradaic efficiency of > 95% measured by ICP-MS for MnO_2 electrodeposition (Table SI3-1), the continuous linear variation suggests the faradaic efficiency holds along the whole charge.

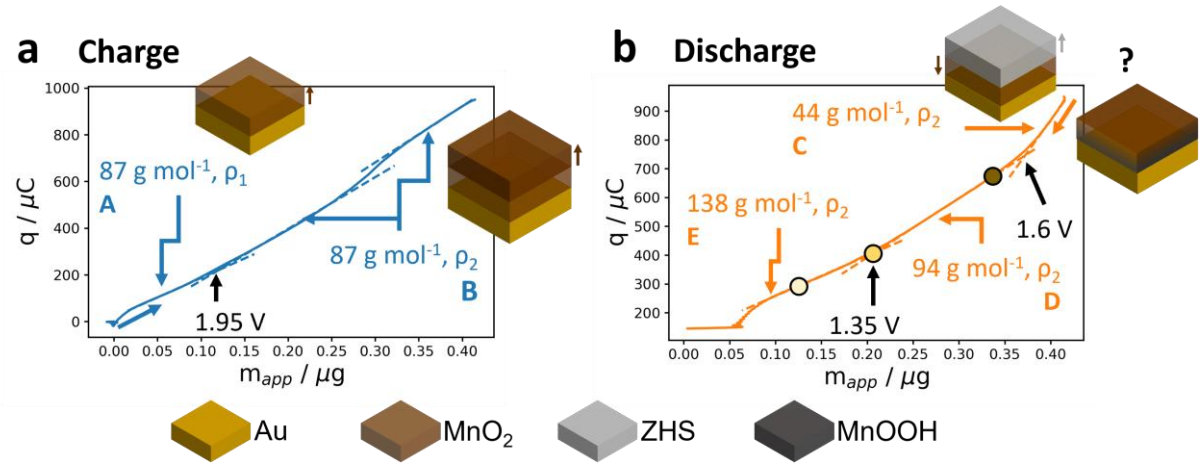

Figure 3. Charge vs apparent mass plot during a) charge and b) discharge in the ZHS-saturated electrolyte (experiment presented in Figure 2d-f). Dashed lines represent local slopes. The corresponding molar masses are given alongside. The same plot for the unsaturated electrolyte is given in **Figure SI7**.

As explained above, the linear charge-mass relationship enables estimating the apparent molar mass, M_{app}, of the deposit according to Faraday's law:

$$q = \frac{2F}{M_{app}} m_{app} = \frac{2F\rho_{app}S}{M_{app}} \delta_{app}. \quad (6)$$

In order for the slope in region A (from 0.85 to 1.95 V in the forward scan) to match with the molar mass of MnO_2, a density of $\rho_{app} = \rho_1 = 1.62$ g cm^{-3} has to be used in the conversion. This value is approximately three times smaller than the density of bulk MnO_2 ($\rho_{bulk} = 5.03$ g cm^{-3}), but close to the actual density of the film determined by ellipsometry and ICP-MS ($\rho_{meas} = 1.95 \pm 0.35$ g cm^{-3}, **Table SI4-2**), as well as to previously reported densities of electrodeposited MnO_2.[61] This rather low density is also supported by SEM images of the film which reveal a high degree of porosity (**Figure SI8**).[41,42,62] If the pores are filled with electrolyte trapped inside the film during electrodeposition, it would be more difficult to determine the true molar mass of MnO_2 using an EQCM as the frequency response would be strongly influenced by these electrolyte pockets.[23,31] Optical reflectometry, however, should

not be affected by such pockets as their refractive index should be very close to that of bulk electrolyte.

Beyond 1.95 V (region B in Figure 3a), the apparent molar mass decreases to 66 g mol^{-1} if the same apparent density is used for the conversion. However, according to the overall faradaic efficiency, MnO_2 should be electrodeposited during the whole charge (see above). Therefore, the apparent density of the MnO_2 film likely increases in region B (ρ_2 = 2.14 g cm^{-3}). This is corroborated by the fact that the actual density of the MnO_2 film measured by ellipsometry and ICP-MS at the end of the charge is very close to the mass-weighted average of ρ_1 and ρ_2 (ρ_{mean} = 1.98 g cm^{-3}, **Table SI4-3**). The charge jump observed between 2.05 and 2.15 V likely corresponds to the formation of a small amount of gold oxide (see blank CV in **Figure SI9**b). Its influence is however limited as the slope quickly gets back to its previous value. Altogether, optical reflectometry, combined with *ex situ* ellipsometric calibration, allows to quantitatively analyze *in situ* and dynamically the electrodeposition of MnO_2 during charge.

2.3.2. Analysis of the discharge

At the beginning of the discharge (Figure 3b), the apparent molar mass decreases to 44 g mol^{-1} (region C). Then, a first slope discontinuity is observed at approximately 1.6 V (from 44 to 94 g mol^{-1}, region D), and a second one at approximately 1.35 V (from 94 to 138 g mol^{-1}, region E).

The apparent molar mass decrease in region C again suggests that the electrodissolution of MnO_2 proceeds with a low faradaic efficiency: the amount of material removed from the surface is lower than expected considering the injected electrochemical charge. As discussed above in the qualitative analysis, this could be attributed to the occurrence of competing pathways such as the reductive conversion to Mn(III) species (discussed above) or the chemical precipitation of another material. The molar masses are however difficult to attribute, and it is therefore difficult to conclude. This is not surprising as the two steps of both proposed mechanisms probably do not track each other. In this case, the analysis based on a single-component film and Faraday's law is not valid anymore.[23,31] To circumvent these issues, complementary structural and chemical characterizations of the MnO_2 film at different states of discharge are proposed in the following. The knowledge of the composition of the film will indeed allow to refine the optical model and analyze more precisely the reflectivity results of the discharge process.

Complementary chemical and structural analyses: Au substrates were then analyzed *ex situ* by ellipsometry, XRD, FT-IRRAS, and XPS after CV experiments halted at different potentials (≈1.85, 1.65, 1.35, 1.2, and 0.85 V) in the reverse scan. By *ex situ* ellipsometry, it is shown that the apparent optical thickness of the film remains almost constant below 1.65 V (≈ 11 ± 2 nm using the refractive index of MnO_2, Figure SI5b), while it is admitted that MnO_2 should dissolve during this reduction step. This again suggests that the electrodissolution of MnO_2 is accompanied by the deposition of another optically probed material, likely ZHS.

No XRD signature (apart from the substrate) is detected until the end of the CV, where peaks associated to ZHS appear (**Figure 4**b). This is consistent with previous reports suggesting that crystalline ZHS is formed at the latest stages of the discharge.[21–23,25,31,43] The precipitate detected during discharge, either *in situ* by optical reflectometry or *ex situ* by ellipsometry, is therefore most likely amorphous. However, when the partially discharged samples were left to dry in air (in the absence of light) for several weeks, XRD patterns could be detected, such as at 1.2 V (Figure 4a). These were attributed to *swetite* $Zn(OH)_2$ as well as to residual $ZnSO_4.7H_2O$, suggesting the presence of a precipitate composed of Zn^{2+}, HO^-, and SO_4^{2-} ions which is not only residual electrolyte.

The presence of HO^- (3000-3600 cm^{-1}) and SO_4^{2-} (950-1230 cm^{-1}) groups throughout discharge is confirmed by FT-IRRAS (Figure 4c and d).[63] In agreement with the XRD results, the characteristic vibrational bands of ZHS (1150, 1110, and 960 cm^{-1}, brown spectrum in Figure 4d) are only observed at the end of the CV. The hyperfine structure in the 3000-3800 cm^{-1} region (Figure 4c) also suggests a crystallized compound is formed at the end of the discharge.

Likewise, XPS measurements on the same samples confirm the presence of Zn and S throughout discharge with a Zn/S ratio greater than 1 (which would correspond to $ZnSO_4$ from the electrolyte) but reaching 4 (which corresponds to crystalline ZHS) only at the end of the CV (Figure 4e). The crystallization of ZHS from $Zn(OH)_2$ is further evidenced by the shift of the Zn2p and O1s peaks from a $Zn(OH)_2$-like to a $ZnSO_4$-like environment (**Figure SI10**-2 and 4f).

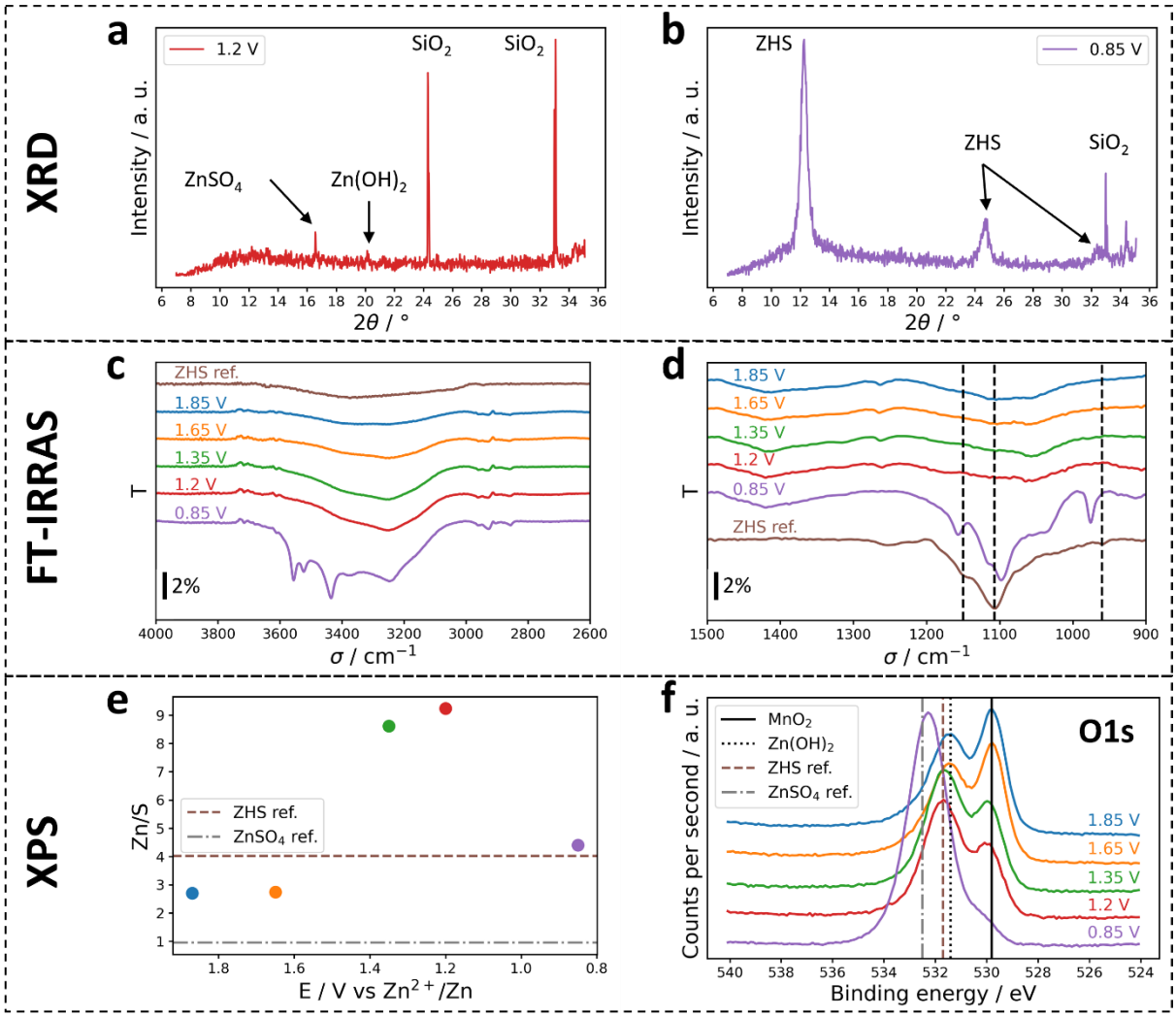

Figure 4. Diffractogram of the MnO_2 electrode cycled a) until 1.2 V in the reverse scan and b) until the end of the discharge. Attributions: $ZnSO_4$ ($ZnSO_4.7H_2O$): (111), PDF 00-001-0402; $Zn(OH)_2$ (*swetite*): (110), PDF 00-001-0360; SiO_2: (-404) and (-512), PDF 00-018-1170); ZHS (zinc hydroxide sulfate hydrate): (001), (002) and (130)-(230), PDF 00-039-0690. FT-IRRA spectra of the electrode at different states of discharge and ATR-FT-IR spectrum of synthesized ZHS powder in the c) high and d) low wavenumber region. e) Zn/S ratio of the electrode measured by XPS at different states of discharge by integrating the Zn2p and S2p peaks. f) High-resolution spectra of the electrode in the O1s region at different states of discharge. The same color code is used for all panels.

All these analyses confirm the presence of a Zn-based precipitate throughout discharge, likely an amorphous form of ZHS, which crystallizes only at the end of the CV for reasons not yet understood.

Quantitative in situ *monitoring*: The detection of ZHS precipitate by different *ex situ* analyses might explain the inadequate fit of the reflectivity data by the simple optical model (Equation 3) taking into account the coating of the electrode as a single component (MnO_2). Thus, a

coating consisting of a mixture of MnO_2 and ZHS, was considered to refine the model. The theoretical reflectivity response of a mixed layer of ZHS and MnO_2 of varying individual composition (thickness or mass density) is then evaluated. It is given as a 2D reflectivity map in **Figure 5**a and used to evaluate, from the experimental reflectivity variations, the proportion of MnO_2 and ZHS during discharge.

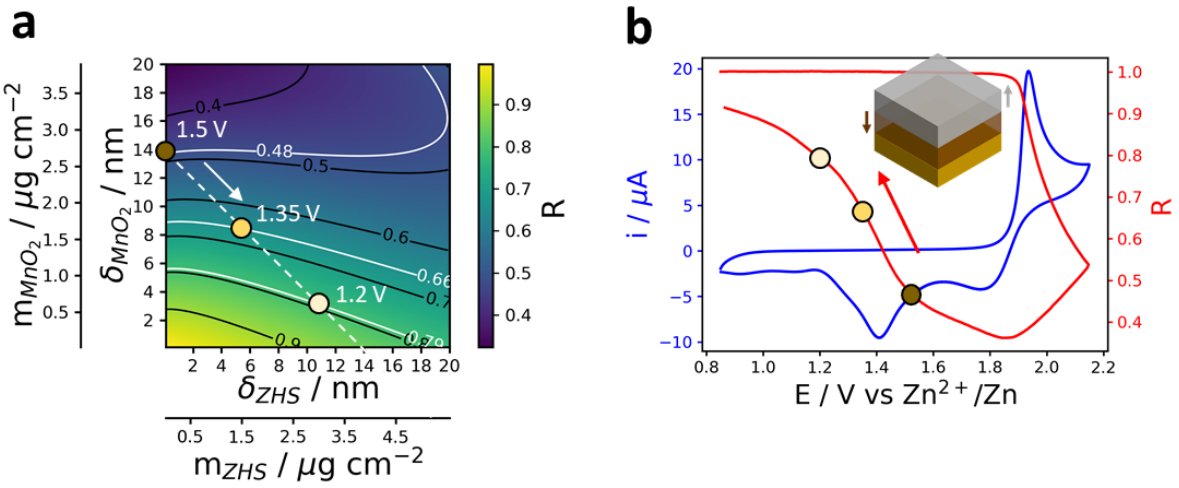

Figure 5. a) Theoretical reflectivity response of a Au substrate covered by a layer of mixed MnO_2 and ZHS of varying individual composition (equivalent thickness or mass density). The white dashed line represents the path followed by the system at a constant apparent thickness. b) Electrochemical CV (blue) and corresponding reflectivity variation (red) of a Au substrate in ZHS-saturated 2 mM $MnSO_4$ + 2 M $ZnSO_4$ (scan rate: 5 mV s^{-1}).

Experimentally, from the slope of the measured reflectivity vs potential in Figure 5b, we see that the electrodissolution of MnO_2 is predominant for E > 1.5 V in the reverse scan. This is fully consistent with the qualitative analysis made before as the precipitate formed between 1.85 and 1.5 V is not stable and therefore does not accumulate on the substrate (Figure SI6). However, it does not necessarily imply that ZHS does not precipitate in this potential region. First, it is assumed that at 1.5 V, the film is mainly composed of MnO_2. This means, for simplicity, that the system is still on the vertical axis in Figure 5a. From the measured reflectivity in Figure 5b, R = 0.48, this corresponds to an apparent MnO_2 thickness of 14 nm, which is in good agreement with the ellipsometric value of 11 nm evaluated from another sample at the same potential. Based on *ex situ* ellipsometry (Figure SI5b), when the electrode potential decreases, the discharge proceeds under roughly constant overall thickness, which means that the reflectivity should evolve following an anti-diagonal line on the 2D reflectivity map in Figure 5a. For the experiment shown in Figure 5b, it should follow the 14 nm constant thickness anti-diagonal represented by the white dashed line in Figure 5a. When the potential

decreases from 1.5 to 1.35, to 1.2 V, the reflectivity rises from 0.48 to 0.66, to 0.79, respectively (Figure 5b).These values are labeled in Figure 5a as the intersection between the dashed white anti-diagonal line and the white iso-reflectivity curves. According to the optical model, this means that at 1.2V, the film is composed of 3.4 nm equivalent thickness of MnO_2 and 10.7 nm equivalent thickness of ZHS, which is in good agreement with ICP-MS measurements (**Table 1**). A good match is also obtained for the sample which was cycled until 1.35 V. The larger error for ZHS than for MnO_2 can be explained by the correction which needs to be applied to the measured Zn concentration (**Table SI4-4**).

Table 1. Comparison between the optical model and ICP-MS measurements.

	Optical model		ICP-MS	
Stop potential [V]	MnO_2 mass [µg cm^{-2}]	ZHS mass [µg cm^{-2}]	MnO_2 mass [µg cm^{-2}]	ZHS mass[a)] [µg cm^{-2}]
1.35	1.6 ± 0.1	1.5 ± 0.6	1.15 ± 0.20	1.35 ± 0.25
1.2	0.7 ± 0.1	3.0 ± 0.7	0.66 ± 0.15	3.00 ± 0.40

[a)] Corrected for the amount of Zn present inside the MnO_2 film (Table SI3-4). $\rho_{MnO2} = \rho_{meas}$ = 1.95 g cm^{-3} (Table SI3-2), ρ_{ZHS} = 2.77 g cm^{-3} for x = 5.[64] Details about uncertainty calculations related to the optical model can be found in SI, section 4.

In summary, the analysis of the reflectivity variations upon the most prominent discharge peak (II) can be mostly understood from a refined optical model considering a two-component film made of MnO_2 and ZHS. It suggests that the compound which precipitates on the substrate upon electrodissolution of MnO_2, as early as at 1.5 V, is consistent with ZHS both from its refractive index and molar mass.

2.4. Galvanostatic cycling

From the careful inspection of oxidation/reduction peaks during CV experiments, it is demonstrated that optical reflectometry allows monitoring *in situ* and quantitatively MnO_2 electrodeposition during charge, as well as the simultaneous electrodissolution of MnO_2 and precipitation of ZHS during discharge. This implies that ZHS is also a key player in the charge process. If so, its role must be manifested on the subsequent charge steps as ZHS accumulates on the electrode after the first and following discharge steps. Moreover, its presence on the discharged electrode should equally play an important mechanistic role during the subsequent charges. This is confirmed experimentally since a single oxidation peak is observed during the first forward scan in CV, as opposed to two oxidation peaks (Figure

SI3b) when a second cycle is recorded. Additionally, the peak potentials are consistent with the two pseudo-plateaus observed under galvanostatic charge (Figure 1b). The appearance of the second oxidation peak could then be related to the presence of ZHS formed during the previous cycle.

2.4.1 Imaging the first galvanostatic charge on a ZHS particle-coated electrode

Our imaging model could here be challenged bearing in mind previous reports [21,24,25,33] on the crystallization of ZHS on the positive electrode at the end of the discharge that is associated to the growth of large and stochastically distributed ZHS crystals. Nevertheless, this situation can be handled by imaging by optical reflectometry the behavior of individual ZHS microparticles immobilized on the bare Au current collector while MnO_2 is electrodeposited and electrodissolved from a ZHS-saturated electrolyte. Optical microscopy was recently used to image heterogeneous Li^+ ion distributions and fluxes within single micrometric particles during cycling,[50] as well as the dissolution of individual $CaCO_3$ biominerals induced by the electrogeneration of acid.[65] In a similar scenario, optical reflectometry images are used here to probe *operando* local material deposition (or equivalently, through the above-proposed optical model, local charging currents) during the first three galvanostatic charge-discharge cycles of the MnO_2 electrode.

Figure 6a shows the optical image of the Au electrode coated with ZHS microparticles, recorded at open circuit in the ZHS-saturated electrolyte. Several micrometric ZHS crystals are clearly detected as dark-contrasted features on this optical image. The smallest optical features visualized are ca. 0.5 µm large, providing an upper limit for the spatial resolution of imaging optical reflectometry (Figure SI1-2). The electrode is then submitted to three galvanostatic charge-discharge cycles while optically monitored *operando*. The optical images are again converted into reflectivity images with the ones corresponding to the first galvanostatic charge-discharge cycle given as a movie in **Supplementary Video 2**. The quantitative single-component optical model analysis discussed earlier at the level of averaged images (such as in Figure 3) is applied here locally to evaluate the local thickness of MnO_2 electrodeposited during charge. To highlight local electrodeposition phenomena, a local MnO_2 thickness is evaluated, $\delta_{MnO2} - \delta_{MnO2,bg}$, relative to a background thickness $\delta_{MnO2,bg}$ measured over a region remote from the particles. The map of such relative local MnO_2 thickness over the whole imaged region is provided in Figure 6b for t = 287 s, while a zoom over a specific particle is presented along different charging times in Figure 6c. Unlike during

the CV study (performed in the absence of ZHS particles), the MnO_2 deposit is not uniform in thickness over the whole Au electrode surface. When the image of the original ZHS particles is overlaid, the regions surrounding the ZHS particles are clearly revealed as regions of higher deposition ($\delta_{MnO2} - \delta_{MnO2,bg} > 0$).

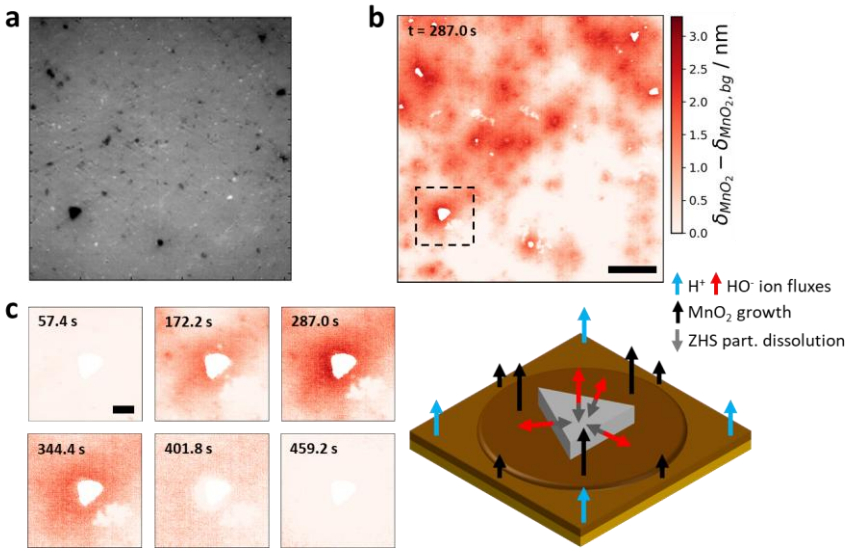

Figure 6. *Operando* imaging of the first galvanostatic charge-discharge cycle of a Zn-MnO_2 battery in ZHS-saturated 2 mM $MnSO_4$ + 2 M $ZnSO_4$. a) Background subtracted optical reflectometry image of the Au cathode coated with ZHS particles (dark-contrasted features). b) Reflectivity image converted into relative MnO_2 thickness, $\delta_{MnO2} - \delta_{MnO2,bg}$. The particles detected in a) are masked to highlight that they are surrounded by regions of thicker MnO_2 deposits. Scale bar: 50 µm. c) Sequential relative MnO_2 thickness images showing the expansion of the excess deposition region around a ZHS particle (zoom inside the dashed region of interest in b)) and schematic mechanistic explanation. Scale bar: 10 µm.

The heterogeneity in local deposition rate is also described from the local variation in optical current (-dR/dt) with time. An example is provided in **Figure 7**a (dark red curve) for the ZHS particle considered in Figure 6c. This local variation is compared to the average evolution of the optical current with time (red curve) over the whole imaged electrode, together with the evolution of the electrode potential. Both local and average optical currents show the same evolution at first: the optical current increases, as expected for an electrodeposition process, rapidly reaching a steady value, until it starts to decrease after about 200 s and the local behavior starts to differ from the average behavior. While the optical current averaged over the whole electrode surface decreases gradually, that of the ZHS particle shows a much steeper decay. Noteworthy, both local and average optical current decays start within the transition of the electrode potential from the first to the second plateau (Figure 7c). It is then

important to decipher these local and average optical behaviors to apprehend mechanistically the origin of the two-plateau charge profile of Zn-MnO_2 batteries as done next.

For the ZHS particle, the steeper optical current decrease corresponds to the particle's dissolution as expected since at the end of the experiment, most particles have disappeared from the raw optical images. By analogy to previous works dealing with the optical monitoring of particles dissolution,[65–67] a particle dissolution onset time, t^0_{diss}, can be defined in our data from the onset of the sharp variation of the optical current. The histogram in Figure 7c shows the distribution of dissolution onset times, t^0_{diss}, for the N = 32 largest individual particles detected in Figure 6a. Once these particles have dissolved (partially at least), for t > 350 s in Figure 6c, the overall surface reflectivity becomes more uniform.

The disappearance of the ZHS particles attests from the electrogeneration of H^+. Indeed, MnO_2 electrodeposition is accompanied by a pH decrease which should thus favor ZHS dissolution (see Equation 1 and 2). The dissolution of the ZHS particles being accompanied by a local release of HO^- ions, they likely play the role of a local pH buffer. Interestingly, the reflectivity images in Figure 6c reveal that the ZHS particle is surrounded by a region of local excess MnO_2 deposition, which can be related to the radial steady-state diffusive release of HO^- ions from the dissolution of the ZHS particle. Also consistent with a local HO^- release from the ZHS particles, Figure 6b shows that (i) the larger the ZHS particle and the larger the area of local MnO_2 deposition, and (ii) regions of high particle density (upper right corner of Figure 6b) show a definite overlap of HO^- diffusion layers. To account for the local MnO_2 film thickness, one should consider that even though a constant overall current is flowing through the current collector, it imposes every part of it is polarized at the same potential. Based on Equation 1, regions of higher local pH, as depicted schematically in Figure 6c, would then provide, at constant potential, regions of higher Mn^{2+} oxidation rates and therefore of higher local deposition rates, equivalently of higher local optical and electrochemical current densities. These observations suggest that such local variation in electrochemical current densities, related to local acidification, are probed by imaging optical reflectometry during MnO_2 electrodeposition.

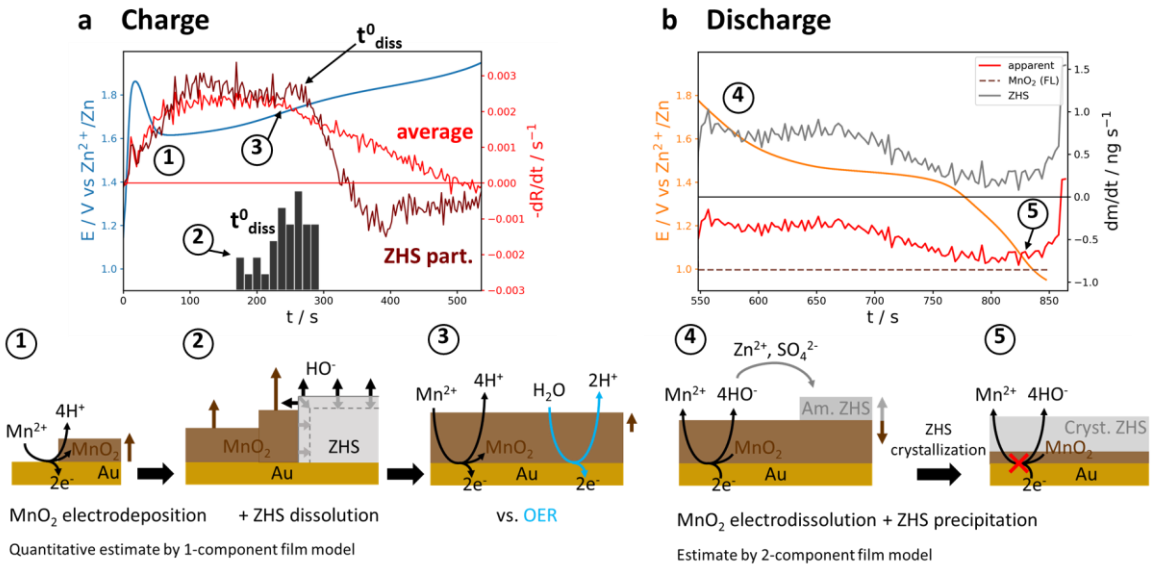

Figure 7. a) Time evolution during charge of the Au electrode potential (blue curve) and of the optical currents (-dR/dt) averaged over the whole image (red curve) or evaluated at the center of the ZHS particle depicted in Figure 6c (dark red curve); histogram of the distribution of dissolution onset times, t^0_{diss}, for N = 32 particles. b) Time evolution during discharge of the Au electrode potential (orange curve) and of the optically inferred average apparent deposition rate (red curve). Dashed brown curve: theoretical MnO_2 dissolution rate derived from Faraday's law (faradaic efficiency: 95%, Table SI4-1). Grey curve: ZHS deposition rate estimated from the apparent and theoretical deposition/dissolution rates. The schemes at the bottom summarize the mechanism revealed optically at each step of the galvanostatic charge-discharge cycle.

Apart from particle dissolution, the average optical current shown in Figure 7a exhibits two distinct trends corresponding to the two potential pseudo-plateaus. MnO_2 is electrodeposited at constant (local or average) current until the second pseudo-plateau at ca. 1.75 V is reached. Using the previously determined reflectivity-mass calibration factor (Figure 3), the optical current can be converted into an apparent deposition rate (expressed in ng s^{-1}). The steady apparent deposition rate is very close to the theoretical MnO_2 deposition rate derived from Faraday's law, confirming the near-100% faradaic efficiency of MnO_2 electrodeposition obtained in CV (Table SI4-1). Interestingly, this is only verified until the ZHS particles start to dissolve i.e., until the electrode surface pH becomes sufficiently acidic to trigger a fast dissolution. Along the second charge domain (for E > 1.75 V or t > 200 s in Figure 7a), the average optical current drops steadily. It suggests that the faradaic efficiency of MnO_2 electrodeposition steadily decreases as the electrode potential increases. This indicates that for E > 1.75 V, MnO_2 electrodeposition competes with another oxidation, most likely water oxidation since at such potentials the thermodynamic stability of water is reached.[44]

$$H_2O \rightarrow 2H^+_{(aq)} + \frac{1}{2}O_{2(aq/g)} + 2e^-. \quad (7)$$

The linear evolution of the faradaic efficiency of MnO_2 electrodeposition then probes the increase of the contribution of water oxidation (either directly at the electrode or through electrocatalysis of MnO_2) with the electrode potential. From the integration of the apparent deposition rate variation with time, the faradaic efficiency of MnO_2 electrodeposition during the whole charge process is ca. 70%. Noteworthy, the shift towards a second charge plateau suggests that the buffer capacity of the electrolyte has been reached. Indeed further charge is accompanied by the dissolution of ZHS particles acting as local solid-state suppliers of HO^-. Once dissolved, the electrolyte pH starts increasing, enabling the competition between MnO_2 electrodeposition and water oxidation. This is in line with *in situ* pH monitoring showing that the shift to the second plateau is associated to an increase in electrolyte pH.[24] It is shown here that this transition is also associated to the decrease of the capacity of the electrode (competition with water oxidation). Such competing reaction is a problem as it shifts, at constant current flow, from a two-proton/one-electron reaction for MnO_2 electrodeposition to a one-proton/one-electron reaction for water oxidation. This explains the gradual pH increase over cycles in the cell, as experimentally demonstrated by *in situ* pH monitoring.[24]

The overall phenomena revealed by *operando* imaging optical reflectometry are summarized in the scheme presented at the bottom of Figure 7a. Particularly, the heterogeneous electrodeposition rates imaged *operando* demonstrate the essential role of ZHS (particles or dissolved in solution) during the charge process: it allows a local buffering of the electrode surface during MnO_2 electrodeposition and a control of its competition with water oxidation. They also suggest that controlling the buffering capacity of the electrolyte i.e., delaying ZHS dissolution, might be an interesting solution towards increasing the capacity of Zn-MnO_2 batteries.

2.4.2 Galvanostatic discharge

The same optical current analysis for the discharge step is provided in Figure 7b. It is characterized by an overall dissolution process ($-dR/dt < 0$) occurring homogeneously over the electrode surface. However, as discussed in the CV study, the apparent dissolution rate is constantly below (in absolute value) the theoretical MnO_2 dissolution rate, meaning that ZHS precipitates throughout the entire discharge. A quantitative analysis of the deposition/dissolution rates is provided. Given that the reflectivity of a Au substrate is ca.

1.45 times less sensitive to ZHS compared to MnO_2 based on the two-component optical model (from Figure 5a), the ZHS deposition rate (grey curve in Figure 7b) can be estimated by the difference between the theoretical MnO_2 electrodissolution rate and the optically inferred dissolution rate. The ZHS deposition rate (ca. 0.3-0.8 ng s^{-1}) is comparable to that of MnO_2 dissolution (0.8 ng s^{-1}), confirming the CV discharge upon approximately constant material thickness. However, this value corresponds only to $1/5^{th}$ of the stoichiometric amount of ZHS expected according to Equation 1 and 2 (for x = 5). Moreover, one can notice a sharp increase in the ZHS deposition rate at the end of the discharge, which could suggest the slow dynamics of ZHS crystallization. These arguments are in agreement with a kinetic control of the precipitation of ZHS: local oversaturation of the solution close to the electrode is mandatory to allow precipitation. This also explains why accurate molar masses cannot be measured by EQCM.

2.4.3 Subsequent cycles

Over the second cycle, the largest particles may show again some localized higher activity regions, but more sporadically and with lesser amplitude. The heterogeneity has completely faded out at the level of the third cycle (as suggested by the images of Figure 1b) as the particles have been completely removed from the electrode surface. The image-averaged optical current variation with time during the third cycle is presented in **Figure SI11**. It essentially shows the same trends as for the first cycle but on a homogeneous surface. It also suggests the dissolution of the homogeneous ZHS precipitate already during the first plateau.

Overall, imaging such repetitive charge-discharge cycles demonstrates that these cycles are smoothing the electrode surface activity and yielding a homogeneous ZHS layer deposition and dissolution.

3. Conclusion

Optical reflectometry is used to monitor qualitatively and quantitatively charge-transfer-induced chemical precipitation/dissolution events in aqueous Zn-MnO_2 batteries. The overall results obtained by this method are summarized in the bottom scheme of Figure 7. Overall, like sensorgrams in SPR microscopy, the variation of the reflectivity with the electrode potential or current during charge-discharge cycles provides a dynamic *in situ* measurement of the amount of material deposited onto (or removed from) the electrode. Like in a classical EQCM analysis, the exchanged charge and mass change are compared to identify the nature

of the electrodeposited/electrodissolved materials or the faradaic efficiency of the underlying processes. Even if all molar masses could not be attributed, it is shown that along with the electrodeposition/electrodissolution of MnO_2, a precipitate is also dissolved/deposited.

Indeed, associated charge and mass change are not perfectly correlated. In this case, unlike the mass change of an EQCM, the optical reflectivity can still be analyzed, through a refined optical model, to extract *in situ* and dynamically quantitative information about the composition of the MnO_2 electrode at a given state of discharge. If the poor correlation between charge and mass change could also be due to a kinetic lag between MnO_2 reduction and net material removal from the electrode, combined with *ex situ* XRD, FT-IRRAS, and XPS analyses of the electrode's chemical composition, optical reflectometry suggests the continuous deposition of ZHS during the entire discharge and especially during the first discharge plateau, in an amorphous form, most likely the reason why its presence through the first discharge plateau was overlooked. Since MnO_2 electrodeposition/electrodissolution is shown to be the main pathway for charge storage, the two different ZHS precipitates (amorphous and crystalline) might be the origin of the two discharge plateaus. This would mean that by favoring or preventing crystallization, one of the two plateaus could be suppressed, thus easing the commercialization of aqueous Zn-MnO_2 batteries.

Optical reflectometry is then used in its imaging mode to probe the role of ZHS during the charge process. The electrodeposition of MnO_2 during charge is imaged on an electrode coated with micrometric ZHS particles, enabling to reveal the role of ZHS during charge. It is then shown that MnO_2 electrodeposition is accompanied by the dissolution of the ZHS particles. These particles act as a solid-state pH buffer or HO^- reservoirs which upon dissolution will locally release HO^- ions. This can be imaged optically as local MnO_2 deposition rates. It is then clearly demonstrated that the two charge plateaus, whose origin has been frequently questioned, are due to a pH change at the electrode surface, the second plateau also revealing the competition between MnO_2 electrodeposition and water oxidation. Here, retarding ZHS dissolution (increasing the buffer capacity) could be a solution towards increasing the capacity of Zn-MnO_2 batteries.

Altogether, this study provides a deep understanding of the ZHS precipitation/dissolution equilibrium. Since MnO_2 electrodeposition/electrodissolution is always accompanied by dramatic pH changes, this equilibrium cannot be omitted. The different ZHS precipitates

highlighted in this work underline the complexity and fragility of this equilibrium, which will hopefully guide future research towards more efficient aqueous Zn-MnO_2 batteries. Although we are well aware that this study was carried in conditions far from practical conditions in terms of concentration, masses and so on, it shows how optical microscopy strategies enabling an *operando* monitoring of local electrochemical processes can be applied to mechanistically understand and improve aqueous Zn-MnO_2 batteries.

Materials and experimental methods

Materials: $ZnSO_4.7H_2O$ (98%), $MnSO_4.H_2O$ (99%), and carbon powder (Super P®, > 99%) were bought from Alfa Aesar and used as received. HNO_3 (Suprapur®, 65%), H_2O_2 (Suprapur®, 30%), H_2SO_4 (ACS reagent, 95.0-98.0%), and KOH (ACS reagent, > 85%) were bought from Sigma-Aldrich and used as received. Solutions were prepared with ultrapure water provided by a Milli-Q® system (Merck Millipore, 18.2 MΩ cm). ZHS-saturated solutions were prepared by adding an excess of chemically synthesized ZHS (see below) to the solution, stirring it for several hours, and gravity filtrating the supernatant.

$Zn_4(OH)_6SO_4.xH_2O$ (ZHS) was prepared by adding a 2 M KOH solution to a 2 M $ZnSO_4$ solution until the pH exceeded 5.2.[68] If the pH became too alkaline, ZHS would be converted to soluble $Zn(OH)_4^{2-}$.[69] The white precipitate was recovered by centrifugation and dried under vacuum at 100°C for a few days. It was then characterized by XRD as being *osakaite* ZHS (x = 5, PDF 00-060-0655).

Au-coated Si wafers (Au(100 nm)/Cr(5 nm)/Si(100)) were either bought from Sigma-Aldrich or prepared in-house by physical evaporation on a bare Si wafer (Sigma-Aldrich). Prior to use, they were soaked in concentrated H_2SO_4 for a few minutes, and then rinsed with copious amounts of water and ethanol.

Galvanostatic cycling in Swagelok cell: 6 mg of carbon powder were deposited on a stainless steel disk (RS), which was then adapted to a two-electrode ½'' PTFA Swagelok cell. A Zn disk (Alfa Aesar) was used as anode, and a glass fiber disk (Whatman®, Sigma-Aldrich) as separator. The separator was soaked with 300 µL electrolyte (0.2 M $MnSO_4$ + 2 M $ZnSO_4$). Galvanostatic cycling of the cell was performed at 30 µA between 0.85 and 1.75 V, using a VMP3 or VMP-300 potentiostat (BioLogic).

Operando *optical reflectometry*: The *operando* optical reflectometry setup was developed in-house and consists of a standard microscope (U-CMAD3, Olympus) equipped with a 40x

water immersion objective (LUMPlanFL N 40x/0.80 W, Olympus) and a CCD camera (MV-D1024E-160-CL-12, Photonfocus). The light source is a halogen white lamp filtered at 490 nm (spectral bandwidth: 20 nm). As depicted in Figure 1b, the substrate is illuminated from the top through the objective, and the reflected light is collected through the same objective. Before each experiment, the tilt of the substrate is adjusted using a Mirau objective (CF Plan 10x/0.30 DI, Nikon) to achieve normal incidence.[70] Such a setup allows 3D spatiotemporal imaging with a sub-micrometer lateral and sub-nanometer vertical resolution.[53] The collected images were treated using homemade MATLAB routines. The relative reflectivity, R, mentioned throughout the text is calculated as:

$$R(t) = \frac{Im(t)}{Im(0)}, \quad (8)$$

where Im(t) represents the raw optical image acquired at time t. Details about the theory are provided in the SI, section 2 and 9.

Electrochemical measurements were performed using a CHI760e potentiostat (CH Instruments), which was triggered manually alongside the camera. Au-coated Si wafers were used as reflective substrate and working electrode (immersed surface area: ca. 0.2 cm^2), a ca. 1x1 cm^2 Au grid (Goodfellow) was used as counter electrode, and a ca. 1x5 cm^2 piece of Zn foil (Alfa Aesar) as reference electrode.

Inductively coupled plasma-mass spectrometry: Inductively Coupled Plasma-Mass Spectrometry (ICP-MS) measurements were performed on a NexION 2000 spectrometer (PerkinElmer) to determine the Mn and Zn content of MnO_2 films at different states of discharge. The films were dissolved in 2 mL of a mixture of 90vol% water, 5vol% HNO_3 and 5vol% H_2O_2 and the resulting solutions were analyzed without further dilution. The ZHS mass calculated from the measured Zn concentration (Table 1) was corrected for the amount of Zn contained in the MnO_2 film (Table SI4-4). As suggested by its low density, some electrolyte might have been trapped inside the film during the electrodeposition (see above).

Fourier-transform infrared reflection-absorption spectroscopy: Fourier-Transform InfraRed Reflection-Absorption Spectroscopy (FT-IRRAS) was performed on a FT/IR-6100 spectrometer (JASCO), with a resolution of 4 cm^{-1}. The substrate itself served as reflective surface for the infrared beam. All spectra were corrected for the background and the presence of water using the Spectra Manager software (JASCO).

X-ray photoelectron spectroscopy: X-ray Photoelectron Spectroscopy (XPS) was performed on a K-Alpha$^+$ spectrometer (ThermoFisher Scientific) using an Al Kα X-ray source (1486.6eV). These measurements were used to determine the Zn/S ratio of MnO_2 films at different states of discharge by integrating the Zn2p and S2p peaks. Unfortunately, the oxidation state of Mn could not be unequivocally determined by this technique as the Mn3s and Mn2p peaks, which are most commonly used for this purpose, overlap with Au and Zn peaks. Still, the position of the Mn2p and Mn3p peaks (Figure SI10-1) suggest that Mn(IV) is directly converted to Mn(II) (and vice versa), but a complex fitting procedure of the Mn3p peak would be necessary to confirm this hypothesis,[71] which is out of the scope of the present study.

X-ray diffraction: X-Ray Diffraction (XRD) was performed on a D8 ADVANCE diffractometer (Bruker) using a Cu Kα X-ray source (1.5406Å). Peaks were attributed using the DIFFRAC.EVA software (Bruker). Enlarged portions of Figure 4a are given in **Figure SI12** to justify the peaks selected for the attributions.

Supporting Information

Supporting Information is available from the Wiley Online Library or from the author.

Acknowledgements

‡L. G. and I. A. contributed equally to this work. L. G. acknowledges the Ecole normale supérieure Paris-Saclay for funding. The authors gratefully acknowledge the ITODYS SEM and XPS facilities, and the Université Paris Cité, Collège de France and CNRS for financial support.

Received: ((will be filled in by the editorial staff))
Revised: ((will be filled in by the editorial staff))
Published online: ((will be filled in by the editorial staff))

References

[1] B. Dunn, H. Kamath, J.-M. Tarascon, *Science (1979)* **2011**, *334*, 928.
[2] J. Rugolo, M. J. Aziz, *Energy and Environmental Science* **2012**, *5*, 7151.
[3] A. Konarov, N. Voronina, J. H. Jo, Z. Bakenov, Y. K. Sun, S. T. Myung, *ACS Energy Letters* **2018**, *3*, 2620.
[4] G. Fang, J. Zhou, A. Pan, S. Liang, *ACS Energy Letters* **2018**, *3*, 2480.
[5] M. Song, H. Tan, D. Chao, H. J. Fan, *Advanced Functional Materials* **2018**, *28*, 1.

[6] B. Tang, L. Shan, S. Liang, J. Zhou, *Energy and Environmental Science* **2019**, *12*, 3288.
[7] X. Zeng, J. Hao, Z. Wang, J. Mao, Z. Guo, *Energy Storage Materials* **2019**, *20*, 410.
[8] H. Li, L. Ma, C. Han, Z. Wang, Z. Liu, Z. Tang, C. Zhi, *Nano Energy* **2019**, *62*, 550.
[9] D. Chen, M. Lu, D. Cai, H. Yang, W. Han, *Journal of Energy Chemistry* **2021**, *54*, 712.
[10] N. Zhang, F. Cheng, Y. Liu, Q. Zhao, K. Lei, C. Chen, X. Liu, J. Chen, *J Am Chem Soc* **2016**, *138*, 12894.
[11] M. H. Alfaruqi, V. Mathew, J. Gim, S. Kim, J. Song, J. P. Baboo, S. H. Choi, J. Kim, *Chemistry of Materials* **2015**, *27*, 3609.
[12] B. Lee, C. S. Yoon, H. R. Lee, K. Y. Chung, B. W. Cho, S. H. Oh, *Scientific Reports* **2014**, *4*, 1.
[13] C. Xu, B. Li, H. Du, F. Kang, *Angewandte Chemie - International Edition* **2012**, *51*, 933.
[14] N. Zhang, F. Cheng, J. Liu, L. Wang, X. Long, X. Liu, F. Li, J. Chen, *Nature Communications* **2017**, *8*, 1.
[15] B. Lee, H. R. Lee, H. Kim, K. Y. Chung, B. W. Cho, S. H. Oh, *Chemical Communications* **2015**, *51*, 9265.
[16] K. Sada, B. Senthilkumar, P. Barpanda, *Journal of Materials Chemistry A* **2019**, *7*, 23981.
[17] S. Zhao, B. Han, D. Zhang, Q. Huang, L. Xiao, L. Chen, D. G. Ivey, Y. Deng, W. Wei, *Journal of Materials Chemistry A* **2018**, *6*, 5733.
[18] Y. Jiang, D. Ba, Y. Li, J. Liu, *Advanced Science* **2020**, *7*, DOI 10.1002/advs.201902795.
[19] M. H. Alfaruqi, J. Gim, S. Kim, J. Song, J. Jo, S. Kim, V. Mathew, J. Kim, *Journal of Power Sources* **2015**, *288*, 320.
[20] C. Xu, S. W. Chiang, J. Ma, F. Kang, *Journal of The Electrochemical Society* **2013**, *160*, A93.
[21] H. Pan, Y. Shao, P. Yan, Y. Cheng, K. S. Han, Z. Nie, C. Wang, J. Yang, X. Li, P. Bhattacharya, K. T. Mueller, J. Liu, *Nature Energy* **2016**, *1*, 1.
[22] B. Lee, H. R. Seo, H. R. Lee, C. S. Yoon, J. H. Kim, K. Y. Chung, B. W. Cho, S. H. Oh, *ChemSusChem* **2016**, *9*, 2948.
[23] L. Liu, Y. C. Wu, L. Huang, K. Liu, B. Duployer, P. Rozier, P. L. Taberna, P. Simon, *Advanced Energy Materials* **2021**, 26.
[24] J. Yang, J. Cao, Y. Peng, W. Yang, S. Barg, Z. Liu, I. A. Kinloch, M. A. Bissett, R. A. W. Dryfe, *ChemSusChem* **2020**, *13*, 4103.
[25] G. Li, Z. Huang, J. Chen, F. Yao, J. Liu, O. L. Li, S. Sun, Z. Shi, *Journal of Materials Chemistry A* **2020**, *8*, 1975.
[26] M. Mateos, N. Makivic, Y. S. Kim, B. Limoges, V. Balland, *Advanced Energy Materials* **2020**, *10*, 1.
[27] D. Chao, W. Zhou, C. Ye, Q. Zhang, Y. Chen, L. Gu, K. Davey, S. Z. Qiao, *Angewandte Chemie - International Edition* **2019**, *58*, 7823.
[28] T. Shoji, M. Hishinuma, T. Yamamoto, *Journal of Applied Electrochemistry* **1988**, *18*, 521.
[29] C. Zhong, B. Liu, J. Ding, X. Liu, Y. Zhong, Y. Li, C. Sun, X. Han, Y. Deng, N. Zhao, W. Hu, *Nature Energy 2020 5:6* **2020**, *5*, 440.
[30] H. Moon, K. H. Ha, Y. Park, J. Lee, M. S. Kwon, J. Lim, M. H. Lee, D. H. Kim, J. H. Choi, J. H. Choi, K. T. Lee, *Advanced Science* **2021**, *8*, 1.
[31] I. A. Rodríguez-Pérez, H. J. Chang, M. Fayette, B. M. Sivakumar, D. Choi, X. Li, D. Reed, *Journal of Materials Chemistry A* **2021**, *9*, 20766.
[32] O. Fitz, C. Bischoff, M. Bauer, H. Gentischer, K. P. Birke, H. M. Henning, D. Biro, *ChemElectroChem* **2021**, *8*, 3553.

[33] X. Guo, J. Zhou, C. Bai, X. Li, G. Fang, S. Liang, *Materials Today Energy* **2020**, *16*, 100396.
[34] X. Z. Zhai, J. Qu, S. M. Hao, Y. Q. Jing, W. Chang, J. Wang, W. Li, Y. Abdelkrim, H. Yuan, Z. Z. Yu, *Nano-Micro Letters* **2020**, *12*, 1.
[35] Q. Zhao, X. Chen, Z. Wang, L. Yang, R. Qin, J. Yang, Y. Song, S. Ding, M. Weng, W. Huang, J. Liu, W. Zhao, G. Qian, K. Yang, Y. Cui, H. Chen, F. Pan, *Small* **2019**, *15*, 1.
[36] G. Liu, H. Huang, R. Bi, X. Xiao, T. Ma, L. Zhang, *Journal of Materials Chemistry A* **2019**, *7*, 20806.
[37] J. Huang, Z. Wang, M. Hou, X. Dong, Y. Liu, Y. Wang, Y. Xia, *Nature Communications* **2018**, *9*, 1.
[38] W. Sun, F. Wang, S. Hou, C. Yang, X. Fan, Z. Ma, T. Gao, F. Han, R. Hu, M. Zhu, C. Wang, *J Am Chem Soc* **2017**, *139*, 9775.
[39] N. Qiu, H. Chen, Z. Yang, S. Sun, Y. Wang, *Electrochimica Acta* **2018**, *272*, 154.
[40] Y. Li, S. Wang, J. R. Salvador, J. Wu, B. Liu, W. Yang, J. Yang, W. Zhang, J. Liu, J. Yang, *Chemistry of Materials* **2019**, *31*, 2036.
[41] G. M. Jacob, I. Zhitomirsky, *Applied Surface Science* **2008**, *254*, 6671.
[42] W. H. Ryu, J. H. Yoon, H. S. Kwon, *Materials Letters* **2012**, *79*, 184.
[43] T. Shoji, T. Yamamoto, *Journal of Electroanalytical Chemistry* **1993**, *362*, 153.
[44] C. F. Bischoff, O. S. Fitz, J. Burns, M. Bauer, H. Gentischer, K. P. Birke, H.-M. Henning, D. Biro, *Journal of The Electrochemical Society* **2020**, *167*, 020545.
[45] B. Chen, H. Zhang, J. Xuan, G. J. Offer, H. Wang, *Advanced Materials Technologies* **2020**, *5*, 2000555.
[46] J.-F. Lemineur, H. Wang, W. Wang, F. Kanoufi, *Annual Rev. Anal. Chem* **2021**, *15*, 1.
[47] F. Kanoufi, in *Encyclopedia of Electrochemistry*, John Wiley & Sons, Ltd, **2021**, DOI 10.1002/9783527610426.bard030108.
[48] X. Ye, M. Saqib, J. Mao, G. Li, R. Hao, *Cell Reports Physical Science* **2021**, *2*, DOI 10.1016/j.xcrp.2021.100420.
[49] D. Jiang, Y. Jiang, Z. Li, T. Liu, X. Wo, Y. Fang, N. Tao, W. Wang, H.-Y. Chen, *J Am Chem Soc* **2017**, *139*, 186.
[50] L. Sun, D. Jiang, M. Li, T. Liu, L. Yuan, W. Wang, H.-Y. Chen, *Analytical Chemistry* **2017**, *89*, 6050.
[51] V. Brasiliense, J. Clausmeyer, P. Berto, G. Tessier, C. Combellas, W. Schuhmann, F. Kanoufi, *Analytical Chemistry* **2018**, *90*, 7341.
[52] A. J. Merryweather, C. Schnedermann, Q. Jacquet, C. P. Grey, A. Rao, *Nature* **2021**, *594*, 522.
[53] S. Chakri, A. N. Patel, I. Frateur, F. Kanoufi, E. M. M. Sutter, T. T. M. Tran, B. Tribollet, V. Vivier, *Analytical Chemistry* **2017**, *89*, 5303.
[54] G. Hass, L. Hadley, in *American Institute of Physics Handbook* (Ed.: O.F. Gray), McGraw-Hill, New York, **1972**, pp. 118–160.
[55] S. Bodoardo, J. Brenet, M. Maja, P. Spinelli, *Electrochimica Acta* **1994**, *39*, 1999.
[56] Z. Rogulski, H. Siwek, I. Paleska, A. Czerwiński, *Journal of Electroanalytical Chemistry* **2003**, *543*, 175.
[57] O. G. Tsiklauri, T. A. Marsagishvili, G. S. Tsurtsumiya, S. A. Kirillov, D. I. Dzanashvili, *Russian Journal of Electrochemistry* **2008**, *44*, 1299.
[58] W. M. Haynes, D. R. Lide, T. J. Bruno, *CRC Handbook of Chemistry and Physics*, CRC Press, **2016**.
[59] B. J. Hertzberg, A. Huang, A. Hsieh, M. Chamoun, G. Davies, J. K. Seo, Z. Zhong, M. Croft, C. Erdonmez, Y. S. Meng, D. Steingart, *Chemistry of Materials* **2016**, *28*, 4536.
[60] B. A. Prabowo, A. Purwidyantri, K. C. Liu, *Biosensors (Basel)* **2018**, *8*, DOI 10.3390/bios8030080.
[61] E. Preisler, *Journal of Applied Electrochemistry* **1976**, *6*, 301.

[62] X. Dai, M. Zhang, J. Li, D. Yang, *RSC Advances* **2020**, *10*, 15860.
[63] G. Socrates, *Journal of Raman Spectroscopy* **2001**, 347.
[64] L. S. Germann, R. E. Dinnebier, X. Liu, Y. Dong, W. Li, *Zeitschrift fur Anorganische und Allgemeine Chemie* **2016**, *642*, 255.
[65] M. Yang, C. Batchelor-McAuley, S. Barton, R. E. M. Rickaby, H. A. Bouman, R. G. Compton, *Angewandte Chemie - International Edition* **2021**, *60*, 20999.
[66] V. Brasiliense, A. N. Patel, A. Martinez-Marrades, J. Shi, Y. Chen, C. Combellas, G. Tessier, F. Kanoufi, *J Am Chem Soc* **2016**, *138*, 3478.
[67] A. N. Patel, A. Martinez-Marrades, V. Brasiliense, D. Koshelev, M. Besbes, R. Kuszelewicz, C. Combellas, G. Tessier, F. Kanoufi, *Nano Letters* **2015**, *15*, 6454.
[68] A. Moezzi, M. B. Cortie, A. M. McDonagh, *Dalton Transactions* **2013**, *42*, 14432.
[69] B. Beverskog, I. Puigdomenech, *Corrosion Science* **1997**, *39*, 107.
[70] S. Munteanu, J. P. Roger, Y. Fedala, F. Amiot, C. Combellas, G. Tessier, F. Kanoufi, *Faraday Discussions* **2013**, *164*, 241.
[71] E. S. Ilton, J. E. Post, P. J. Heaney, F. T. Ling, S. N. Kerisit, *Applied Surface Science* **2016**, *366*, 475.